Contents lists available at ScienceDirect

Inorganic Chemistry Communications

journal homepage: www.elsevier.com/locate/inoche

Short communication

Sunlight active photocatalytic studies of Fe_2O_3 based nanocomposites developed via two-pot synthesis technique

Archana Venkatachalam [a], John Abel Martin Mark [a], Deivatamil D [b], Revathi J [c], Joseph prince Jesuraj [a,*]

[a] Department of Physics, University College of Engineering, Bharathidasan Institute of Technology Campus, Anna University, Tiruchirappalli 24, Tamil Nadu, India
[b] Department of Physics, Periyar E.V.R. College, Tiruchirappalli 23, Tamil Nadu, India
[c] Department of Physics, St. Antony's College of Arts and Sciences for Women, Ammakulathupatti, Tamil Nadu 624005, India

ARTICLE INFO

ABSTRACT

The $Fe_2O_3@MgO$, $Fe_2O_3@Mn_2O_3$, and $Fe_2O_3@Co_3O_4$ nanocomposites were developed using a two-pot wet chemical procedure. The structure and the phase were confirmed using the Powder X-Ray diffraction tool (PXRD). The optical properties of the prepared materials were analyzed using Photoluminescence (PL) and Diffuse Reflectance Spectroscopy (DRS) technique. Surface morphology and elemental composition of the prepared samples were studied by Scanning Electron Microscope (SEM) and Energy Dispersive X-Ray Spectroscopy (EDAX). The porosity and the surface area of the materials were studied by Brunauer–Emmett–Teller (BET) analysis. The functional group present in the prepared material is analyzed by Fourier transforms IR analysis (FT-IR). The photocatalytic analysis was done using Methylene Blue (MB), Rhodamine B (RhB) and Phenol. Further the mineralizations of the pollutants are studied by COD experiment and also the radical scavenger experiments are carried out.

1. Introduction

Because of their better magnetic, chemical, optical, electronic properties, and large surface to volume ratio, the semiconducting micro, and nanomaterials have attracted research interest in vast areas [1–3]. The semiconducting materials can be used in various application fields such as photo-electric devices, catalysis, gas sensing devices, in the field of medicine like drug delivery, imaging, and also as a drug, and for energy storage devices like supercapacitors, batteries, etc. Among the other global issues, water pollution and scarcity is a top-listed; which has acute problem owing to rapid urbanization and industrialization. Several industries like photography, printing, food, dyeing, cosmetics, and textile develop man-made organic compounds that are greatest perilous to the environment because of low degradability, eco-toxic, and carcinogenic nature [4]. From the industries, above 20% of dyes are ejected as effluents during various processes such as dyeing, bleaching, etc; into the surroundings through numerous routes which have shown nearly 10–15% of the severe effect on aquatic life as well as on public health [5]. Therefore, it is necessary to degrade or remove the effluents from industries for purifying the contaminated water. Several methods have arrived for the treatment of industrial effluents in water namely membrane filtration, aerobic oxidation, ion-exchange, reverse osmosis, liquid–liquid extraction adsorption, ultra filtration, chlorination, bio-sorption, and advanced oxidation processes (AOPs) like ozonation, photolysis, and heterogeneous photocatalysis [6,7].

Advanced oxidation process (AOPs) is one of the most attractive approaches that are extensively utilized for the decontamination of wastewater due to its non- selectiveness, higher efficiency, low energy consumption, and has a capability for complete degradation of biological and organic pollutants [8,9]. The principle of AOP is that the formation of hydroxyl radical (OH•) that is highly reactive and is responsible for the complete mineralization of organic contaminants [10]. The heterogeneous photocatalysis technique is deemed to be one of the attractive AOP approaches [11–16]. In this process, a high energy light photon is absorbed by the photocatalyst material usually a semiconductor, which in turn, produces strong oxidation agents such as hydroxyl radical (OH•) and superoxide anions (O_2^-). Hence these reactive species will degrade the pollutants and mineralize it [17]. Semiconductor materials have been vastly utilized as an effective photocatalyst for the decontamination of organic pollutants from
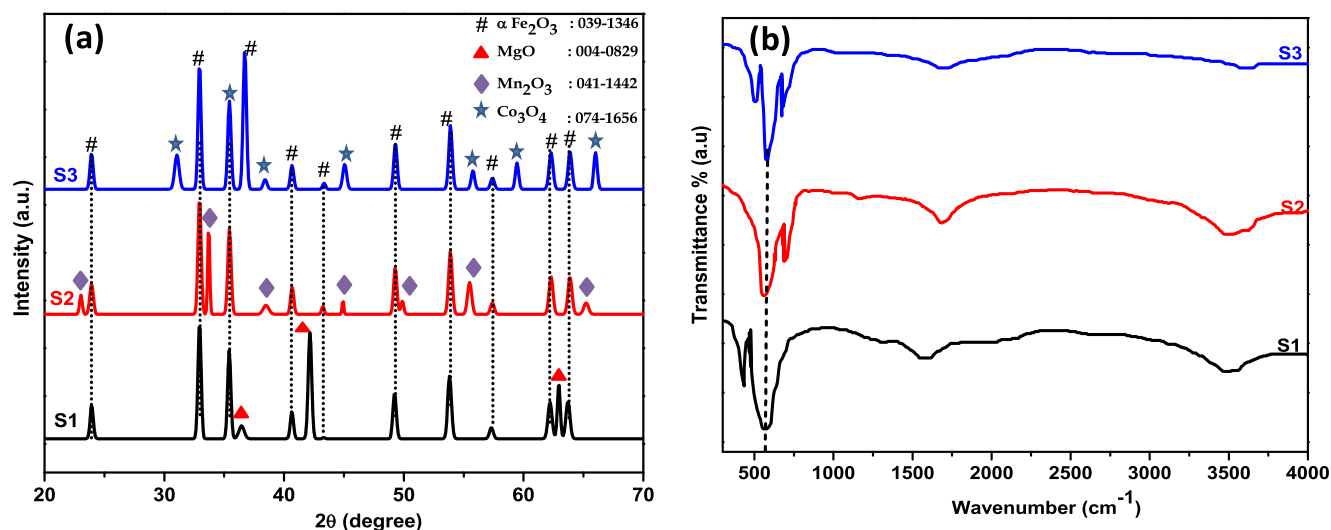
Fig. 1. (a) PXRD patterns of the prepared samples (b) FT-IR spectra of the prepared samples.

wastewater owing to its high charge transferring capability, under visible or UV light irradiation [18–20]. However, in practice, the utility of semiconductor materials as photocatalyst are restricted to some extent because of the quick recombination of photogenerated electron-hole pairs, reduced electrical conductivity, poor visible light responses, photo-corrosion, and inefficient solar-light absorption, [21,22]. Fe_2O_3 is a kind of semiconducting photocatalyst, is considered to be an effective visible-light-driven photocatalyst due to its better chemical stability, high crystallinity, cost-effective, facile production, high specific surface area, eco-friendliness, and absorbs the majority of the visible light due to its narrow bandgap [23,24]. Although it has extraordinary properties, this iron oxide nanoparticle has been getting into constraint due to the faster recombination rate of photogenerated electron-hole pairs. To overcome this many researchers have made a strategy to combine other metals, metal oxides, metal sulfides, also carbonaceous materials with iron oxide. This is because of the incorporation of other material as an impurity or a heterogeneous structure will improve the electron-hole separation of Fe_2O_3. For instance, Jun Liu et. al., had attempted to synthesize Fe_2O_3@TiO core–shell nanocomposite, and achieve a better photocatalytic activity in Rhodamine B dye degradation [25]. Juan Xie et al., have prepared Fe_2O_3@ZnO nanocomposite, for the photocatalytic application to degrade pentachlorophenol [26]. The mixture of carbonaceous and metal sulfide with Fe_2O_3 nanoparticle will also enhance the photocatalytic activity [23,27]. On the other hand, MgO, Mn_2O_3, and Co_3O_4 are also widely utilized as a photocatalyst for wastewater treatment [28–33]. Hence, this work aims to prepare the combinations of those materials with Fe_2O_3 and to comparatively study the optical, and photocatalytic behaviors of the prepared materials.

There are several methods evolved for the synthesis of nanomaterials to date, namely hydrothermal, sol–gel, micro-emulsion, ball milling, microwave-assisted, solid-state synthesis, electrochemical approach, co-precipitation, etc,. The co-precipitation technique is one of the facile techniques for synthesizing nanomaterials. In this method, there is no need of high-tech instrumentation and laboratories, temperature control during the reaction is easy, easy to maintain pH value, no initial steps for the preparation of precursors, suitable for synthesizing almost all type of materials, high yield at a time, cost-effective, etc. Herein, the composites of Fe_2O_3@MgO, Fe_2O_3@Mn_2O_3, and Fe_2O_3@Co_3O_4 materials were developed through the chemical co-precipitation route. The structural, optical, morphological properties of the prepared samples are analyzed and discussed in the following sections. The photocatalytic activity of the prepared materials was experimentally examined by degrading the organic pollutant Rhodamine B and Methylene Blue dye. Various

parameters influencing the photocatalytic activity was measured experimentally.

1.1. Materials

The precursor salts used for making Fe_2O_3@MgO, Fe_2O_3@Mn_2O_3 and Fe_2O_3@Co_3O_4 composite materials are Iron (III) chloride hexahydrate ($FeCl_3 \cdot 6H_2O$), Magnesium chloride hexahydrate ($MgCl_2 \cdot 6H_2O$) Cobalt (II) chloride hexahydrate ($CoCl_2 \cdot 6H_2O$) and Manganese chloride tetra-hydrate ($MnCl_2 \cdot 4H_2O$), which are brought from Merck product with 99% purity. Sodium hydroxide pellets (NaOH) is used as a precipitation agent, Double distilled water (DD) is used as a solvent and Cetyl trimethyl ammonium bromide (CTAB) ($C_{19}H_{42}BrN$) is used as a surfactant for composite preparation. All those chemicals are directly utilized in the synthesis process without further purifications. For photocatalytic water treatment, Methylene Blue (MB) ($C_{16}H_{18}ClN_3S$) and Rhodamine B (RhB) ($C_{28}H_{31}ClN_2O_3$) organic dyes are used as a pollutant.

1.2. Synthesis procedure

The synthesis procedure carried out for synthesizing Fe_2O_3@MgO, Fe_2O_3@Mn_2O_3, and Fe_2O_3@Co_3O_4 composite materials are as follows: 0.05 M of ($FeCl_3 \cdot 6H_2O$) was dissolved in 100 ml of DD water. 10 ml aqueous solution of 4 M NaOH was added drop by drop into the above solution with the help of the burette. The solution was kept under continuous vigorous stirring for 6 h after the addition of NaOH. After the stirrer stopped, the beaker is kept undisturbed for the whole night to allow the precipitate has been settled down at the bottom of the beaker. The precipitate was washed with ethanol using filter paper until the pH reaches neutral. This obtained wet precipitate is poured into 100 ml of DD water and stirred. After 10 min of stirring, 0.005 M of CTAB is added to the reaction mixture. 0.05 M of ($MgCl_2 \cdot 6H_2O$) was added and the solution was continuously stirred to obtain a homogenous mixture. Then, a 10 ml aqueous solution of 4 M NaOH was added drop by drop into the above solution with the help of the burette. After the complete addition of the NaOH solution, the reaction mixture was vigorously stirred for the same 6 h and then the beaker containing the reaction mixture is kept undisturbed for the whole night. The obtained precipitate was washed with ethanol for getting the neutral pH and it has been spread in a petri dish and dries in a hot air oven at 80 °C for 12 h. Then the dried powder is grained finely and kept for calcination in a furnace at 700 °C for 3 h. The same procedure was followed step by step for the preparation of Fe_2O_3@Mn_2O_3 and Fe_2O_3@Co_3O_4 composite materials
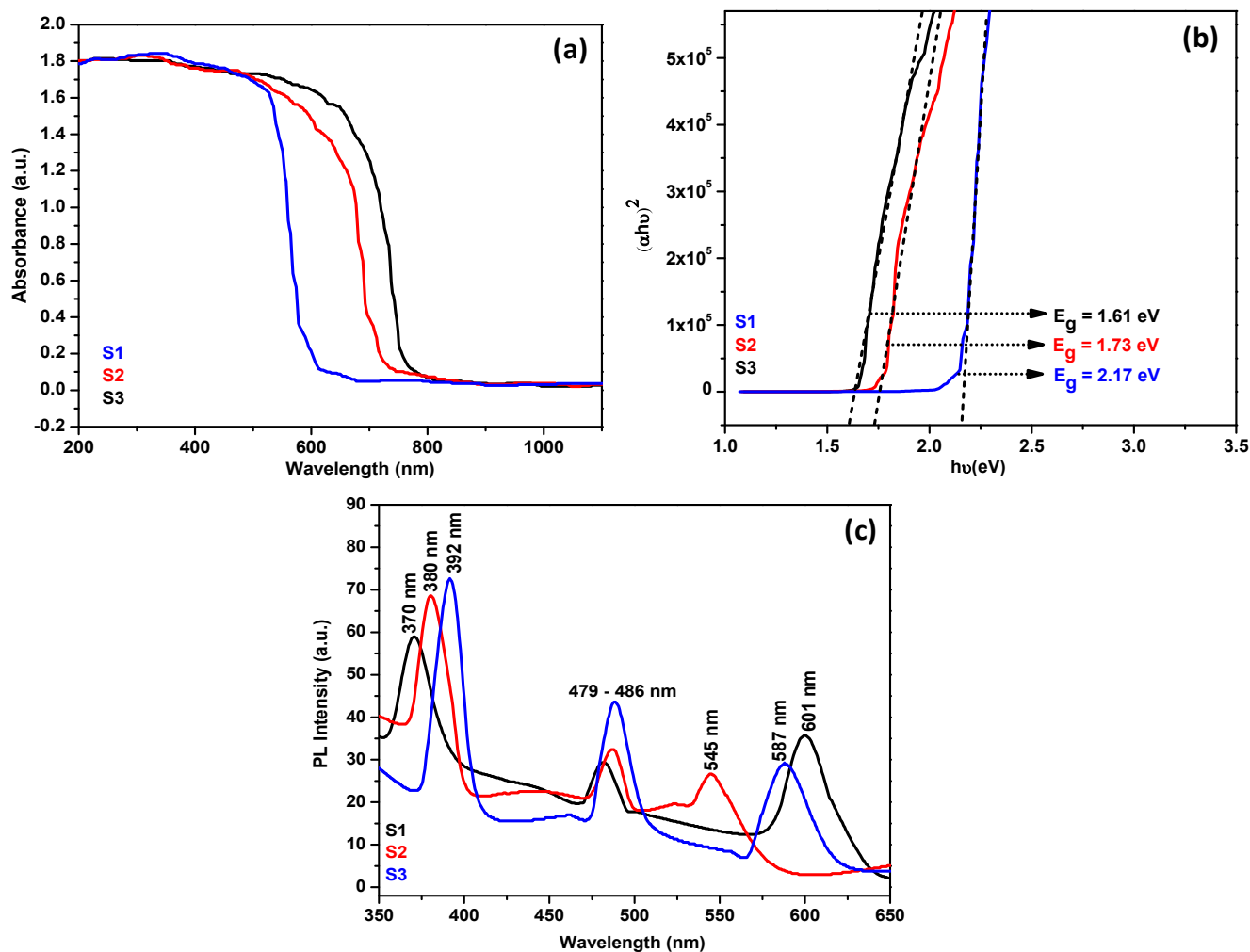
Fig. 2. (a) DRS absorption spectra of the prepared samples. (b) Tauc's plot of the prepared samples. (c) PL spectra of the prepared samples.

by changing the precursors ($MnCl_2 \cdot 4H_2O$) and ($CoCl_2 \cdot 6H_2O$) instead of ($MgCl_2 \cdot 6H_2O$) respectively. The prepared materials Fe_2O_3@MgO, Fe_2O_3@Mn_2O_3, and Fe_2O_3@Co_3O_4 are hereafter captioned as S1, S2, and S3 respectively in the rest of the manuscript.

1.3. Photocatalytic experiment

To scrutinize the photocatalytic activity of the prepared samples 100 ml of 10 mg/l initial concentrations of MB and RhB dye solutions and for Phenol 100 ml of 20 ppm solution are taken and the 0.1 mg of catalyst load was taken. For the light source sunlight was utilized. The beaker containing dye solutions with catalysts was kept under sunlight in an open place such that the light gets focused on the dye solution without any constrains. To utilize the bright efficient sunlight, the experiment was done in a noontime between 11.30 am to 2.00 pm on a perfect sunny day. For the stability check, the used catalyst was utilized repeatedly up to four cycles of fresh dye solutions. The degradation efficiency was calculated by using the following formula,

$$\eta = \left(1 - \frac{c}{c_0}\right) \times 100 \ (\%) \tag{1}$$

C is the concentration of the dye solution taken at every time intervals, C_0 is the initial dye concentration, and η is the calculated degradation efficiency.

2. Results and discussions

2.1. Structural studies

The crystalline nature and phase, average crystallite size, and phase purity of the prepared materials are studied with the obtained PXRD pattern which was shown in Fig. 1. The diffraction spectrum was recorded for 2θ values between 20 and 70°. The diffraction pattern of all the samples S1, S2, and S3 confirms that the prepared materials are composites of α-Fe_2O_3. The peaks observed at 23.7°, 32.7°, 35.1°, 40.4°, 43.3°, 49.1°, 53.6°, 57.1°, 62.2°, 63.5°, and 69.3° corresponding to the planes (0 1 2), (1 0 4), (1 1 0), (1 1 3), (2 0 2), (0 2 4), (1 1 6), (0 1 8), (2 1 4), and (3 0 0) respectively are captioned with (#) in the Fig. 1(a), confirms the formation of hematite α-Fe_2O_3 nanoparticles and well match with the standard JCPDS card: 039-1346 [34]. The pattern reveals the presence of α-Fe_2O_3 in all the prepared samples also in perfect ratios. The S1 pattern in the Fig. 1 corresponds to Fe_2O_3@MgO composite material. From the S1 pattern the peak obtained at 36.9°, 42.8°, and 62.3° associated with (1 1 1), (2 0 0), and (2 2 0) belongs to cubic phase MgO nanoparticles and is well-matched with JCPDS card: 004-0829 [35]. The XRD pattern of the S2 sample furnish the presence of α-Fe_2O_3 by the peaks obtained at the above mentioned 2θ values, along with cubic Mn_2O_3 which is confirmed by the diffraction peaks exists at 23.1°, 32.9°, 38.1°, 45.1°, 49.4°, 55.2°, and 65.6° corresponds to the planes (2 1 1), (2 2 2), (4 0 0), (3 3 2),(4 3 1), (4 4 0) and (6 2 2). This cubic Mn_2O_3 pattern is well agreed with JCPDS card: 041-1442 [36] and this confirms the formation of Fe_2O_3@Mn_2O_3 composite material. The peaks emerge at

31.1°, 36.8°, 38.5°, 45.3°, 55.6°, 59.3°, and 65.2° belongs to the plane (220), (311), (222), (400), (422), (511) and (440) in the pattern S3 reveals the formation of FCC spinel-type Co_3O_4 along with the α-Fe_2O_3 material and is agreed with the JCPDS card: 042-1467 [37]. This proves that the developed material S3 is a composite of Fe_2O_3@Co_3O_4.

The average crystallite size of each material was calculated using the traditional Scherrer formula,

$$D = \frac{K\lambda}{\beta cos\theta} \qquad (2)$$

D is the calculated crystallite size of the material; K is the constant (0.98) called shape factor; λ is an incident X-ray radiation wavelength (CuKα – 1.5406 Å); β is the full width half maximum (FWHM), and θ is an angle of diffraction. From the formula and the obtained peaks of the materials, the average crystallite size of the Fe_2O_3 is achieved to be 38 nm, 44 nm, 46 nm, for S1, S2, S3 nanocomposites respectively. The crystallite size of the MgO, Mn_2O_3, and Co_3O_4 are individually calculated from the observed peaks and are found to be 36 nm, 45 nm, 42 nm, respectively. The XRD pattern didn't show any impurity peaks furnishes the purity of the materials and also the highly intense and sharp predominant peaks reveal the good degree of crystalline nature of the prepared materials. From the XRD analysis, it is concluded that the synthesized materials are the phase pure composites of Fe_2O_3@MgO, Fe_2O_3@Mn_2O_3, and Fe_2O_3@Co_3O_4.

2.2. Fourier transforms IR analysis (FT-IR)

The various functional groups present in the as-prepared samples are examined using the FT-IR analysis technique. Fig. 1(b); shows the FT-IR transmittance spectra of all the three synthesized materials and are mentioned as S1, S2, and S3. From the spectra it is noticed that all the three composite materials exhibit the same transmittance peak at around 569 cm^{-1} which is arrived due to the stretching vibrations of Fe—O molecules [38] and generally the transmittance peaks located in the range of ~1500–1900 cm^{-1} and 3150–3550 cm^{-1} has belonged to the H—O—H bending and stretching mode vibration [39]. Here the peaks arrive in that region is may be due to the surface adsorbed water molecules during the preliminary sample preparing process for FT-IR analysis. Hence it confirms the contribution of Fe_2O_3 nanoparticles in all the prepared samples. Spectrum S1 refers to Fe_2O_3@MgO composite material, from that the transmittance peak obtained at 437 cm^{-1} is belongs to the Mg—O metal–oxygen vibrations [40]. S2 spectrum represents the transmittance curve of Fe_2O_3@Mn_2O_3 nanocomposite material, and the peak emerges at 686 cm^{-1} is due to the vibrations of Mn—O molecules in its stretching mode [41]. The transmittance curve S3 is corresponding to the Fe_2O_3@Co_3O_4 composite, from that there are two more peaks aroused at around 665 cm^{-1} and 514 cm^{-1} other than the common Fe_2O_3 peak. The peak located at 665 cm^{-1} is corresponding to the tetrahedral sites vibrations; whereas 514 cm^{-1} is associated with the vibrations arrived from the octahedral sites of Co—O molecules respectively [42]. Thus it confirms the formation of metal oxide spinel structure Co_3O_4 molecule. From the overall FT-IR results it affirms that the prepared samples are the composite materials of Fe_2O_3@MgO, Fe_2O_3@Mn_2O_3, and Fe_2O_3@Co_3O_4 and is well agreed with the PXRD obtained results.

2.3. Optical studies

(a) Diffuse reflectance spectroscopy (DRS)

The optical properties such as light absorption and the related optical bandgap of the synthesized materials are analyzed using DRS studies in the case of solid or powdered samples. The obtained reflectance spectra of the materials are converted into the absorption spectrum using the
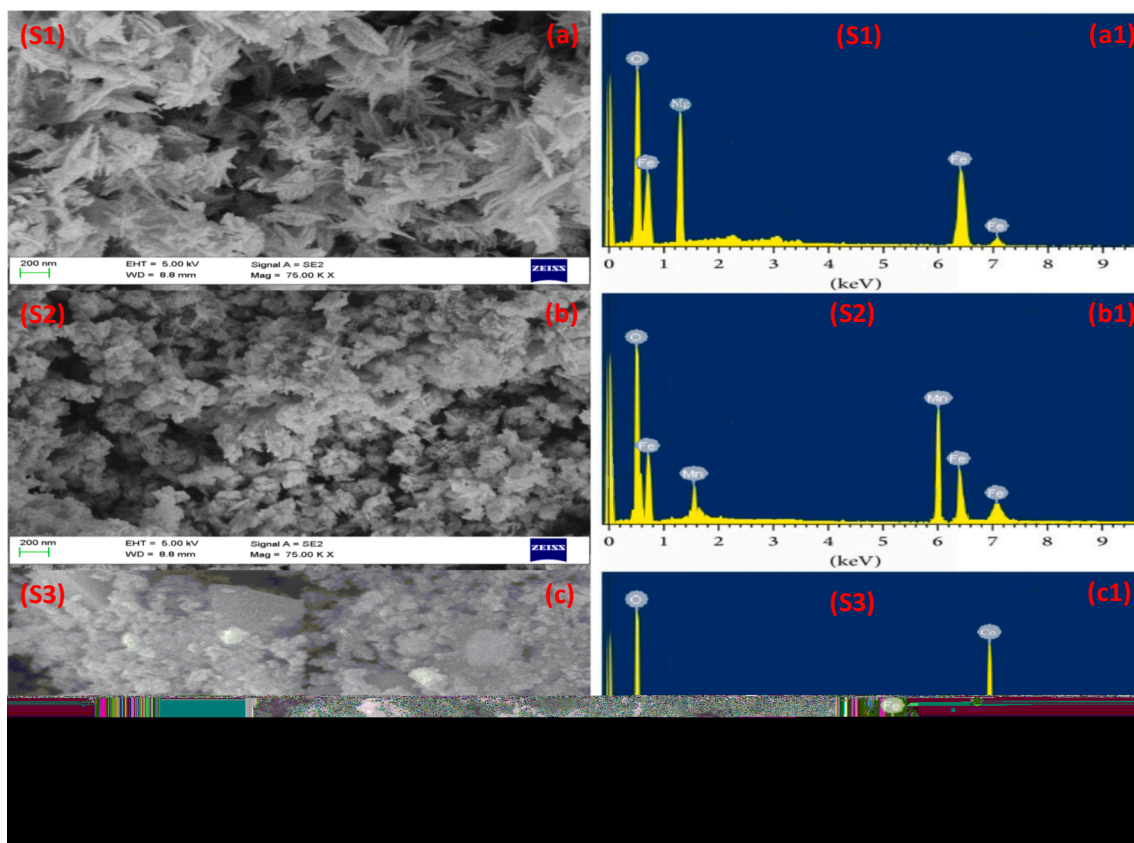

Fig. 3. (a, b, c) SEM micrographs of the prepared samples, and (a1, b1, c1) EDAX spectrum of the prepared samples.

following relation and are shown in Fig. 2(a).

$$F(R) = \frac{1 - R^2}{2R} \tag{3}$$

The spectra were recorded between the 200 nm and 1100 nm wavelength range. From the absorption spectra, the S1 spectrum is shown less absorption range when compared to the other two materials S2 and S3. The optical absorption property of all the three prepared materials were in the order of S1 > S2 > S3. This is because both the Mn_2O_3 as well as Co_3O_4 are narrow bandgap materials like Fe_2O_3 nanoparticles [43–45] so that those materials have not shown much influence in the optical absorption property when it is prepared as a $Fe_2O_3@Mn_2O_3$ and $Fe_2O_3@Co_3O_4$ nanocomposites. But the MgO nanoparticles are generally a wide bandgap material [46] hence it shows more influence in the bandgap of the synthesized $Fe_2O_3@MgO$ composite material. The bandgap of the prepared materials is calculated from their respective absorption spectra using the following relation and by Tauc's plot which is shown in Fig. 2(b).

$$\alpha h\nu = A(h\nu - E_g)^{1/2} \tag{4}$$

where h and A is the Planck's and proportionality constant respectively, α refers to the absorption coefficient, ν is the measure of light in terms of frequency, and E_g is the optical bandgap energy of the material. Using Tauc's plot the bandgap of the synthesized materials is calculated to be 2.17 eV, 1.73 eV, and 1.61 eV for S1, S2, and S3 respectively. From the DRS analysis, it is noted that the S1 material has a larger bandgap value among the three materials. This large bandgap helps to improve the electron-hole separation and hence it will promote the photocatalytic activity of that material.

(b) Photoluminescence studies (PL)

The defects and impurities present in the synthesized materials and the degree of crystallinity of the prepared materials also the range of spectral emission was detected using photoluminescence spectroscopy techniques. Fig. 2(c) illustrates the room temperature PL emission spectra of the prepared samples S1, S2, and S3 recorded in the wavelength ranges from 350 nm to 650 nm. The excitation wavelength used to excite the electrons of the prepared materials is 320 nm. All three materials emit three bands of emissions one in the region of UV and the other two visible bands. The near-band emission in the UV region of wavelength 370 nm, 380 nm, and 392 nm for S1, S2, and S3 respectively is due to the radiative annihilation of surface excitons [47]. The blue band occurs at 479 – 486 nm is owing to the electronic transitions from deep donor levels to the valence band and transitions to the deep level acceptors from the near conduction band-edge [48]. The yellow, green, and orange emission bands located at 587 nm, 545 nm, and 601 nm for S3, S2, and S1 respectively is attributed to the radiative recombination of the electrons from shallow donors with the trapped holes from interstitial oxygen and singly ionized oxygen vacancies [49]. From the PL spectra, it is noticed that the intensity of the emission is less in the UV and blue band region for S1 material and this is because of the large bandgap energy when compared to S2 and S3, but the intensity of peak located at the visible region (601 nm) owing to crystal defects is high. This confirms that the S1 material has more defects like oxygen vacancies and interstitial defects, which will promote more electronic transfer on the surface of the material and thus enhances the photocatalytic activity of that material. Also, all the samples show a high-intensity UV peak which confirms the good crystalline nature of the prepared materials [31] and is well agrees with the PXRD results.

2.4. SEM and EDAX analysis

The surface morphology of the synthesized materials was examined using Scanning electron microscope (SEM) images. Fig. 3 (a, b, c)

Table 1
Elemental composition of the prepared materials.

Materials	Oxygen content (at. %)	Iron content (at. %)	Other atoms content (at. %)
$Fe_2O_3@MgO$ (S1)	52.21	24.01	23.78 (Mg)
$Fe_2O_3@Mn_2O_3$ (S2)	55.17	23.42	21.41 (Mn)
$Fe_2O_3@Co_3O_4$ (S3)	64.36	20.13	15.51 (Co)

represents the SEM micrograph images of S1, S2, and S3 materials at the magnification range of 200 nm. From the SEM images, it is observed that the S1 sample has slightly flake-like morphology and the S2 sample has a plate-like morphology whereas the S3 sample is mostly agglomerated and looks like irregular clusters, but some of them show slightly a spherical structure. The elemental composition of the prepared samples S1, S2, and S3 are analyzed by the EDAX spectrum and shown in Fig. 3 (a1, b1, c1) respectively. The calculated at% of each atom present in the synthesized materials are tabulated in the Table 1.

2.5. BET surface area analysis

The nature of the porosity of the prepared materials as well as the pore size, pore-volume, and the surface area is measured and calculated by Brunauer–Emmett–Teller (BET) analysis technique. Generally, the adsorbing capacity of the samples is measured using various gases as an adsorbent, here the nitrogen (N_2) gas is utilized. Fig. 4 (a, b, c) represents the N_2 adsorption–desorption curve of the synthesized sample S1, S2, S3 respectively. From the adsorption/desorption curve it is observed that all the prepared materials follow the type IV isotherm and the H3 type hysteresis loop. This H3 type hysteresis loop emerges if the nature of the pores present in the prepared materials were slit-type [50]. From these analyses the pore size and pore volume of S1, S2, S3 was calculated to be 40 nm, 27 nm, 22 nm, and 0.404 cm^3/g, 0.279 cm^3/g, 0.224 cm^3/g respectively and is shown in Fig. 4 (d). The BET surface area of S1, S2, and S3 was calculated to be 71.2 m^2/g, 63.5 m^2/g, and 59.8 m^2/g respectively. From this analysis, it is concluded that all the synthesized material has mesoporous nature and exclusively the BET surface area of S1 material was high as compared to the other two materials which promote a maximum number of active sites on the surface of material S1 and hence it enhances the photocatalytic performance of that material.

2.6. Photocatalytic behavior of the prepared materials

The photocatalytic performance of the prepared samples S1, S2, and S3 were comparatively examined by degrading the organic dyes MB & RhB and phenol. In general, the photocatalytic degradation of the dye molecules occurs by the generation of reactive species such as ●OH radicals and O^{2-} anions in different mechanisms. These active species were produced by photolysis (UV treated), and photocatalysis mechanisms, here there is an additional chance of Fenton process is also occurs, because all the prepared materials are the composites of Fe_2O_3 nanoparticles. When the light photons of energy equal to the bandgap energy hit the semiconductor photocatalyst material, the photon energy was absorbed by the free electron in the valence band and it is exciting to the conduction band. Hence the electron-hole separation takes place. The electron in the conduction band now reacts with the oxygen in the aqueous dye solution which in turn produces O^{2-} anions, and the H_2O molecules react with holes that form ●OH radicals.

(a) Reaction kinetics studies

To study the reaction kinetics in the photocatalytic activity of the prepared materials, 3 sets of 100 ml of 10 mg/l concentrations of MB and RhB also 100 ml of 20 ppm solution of phenol was taken separately for
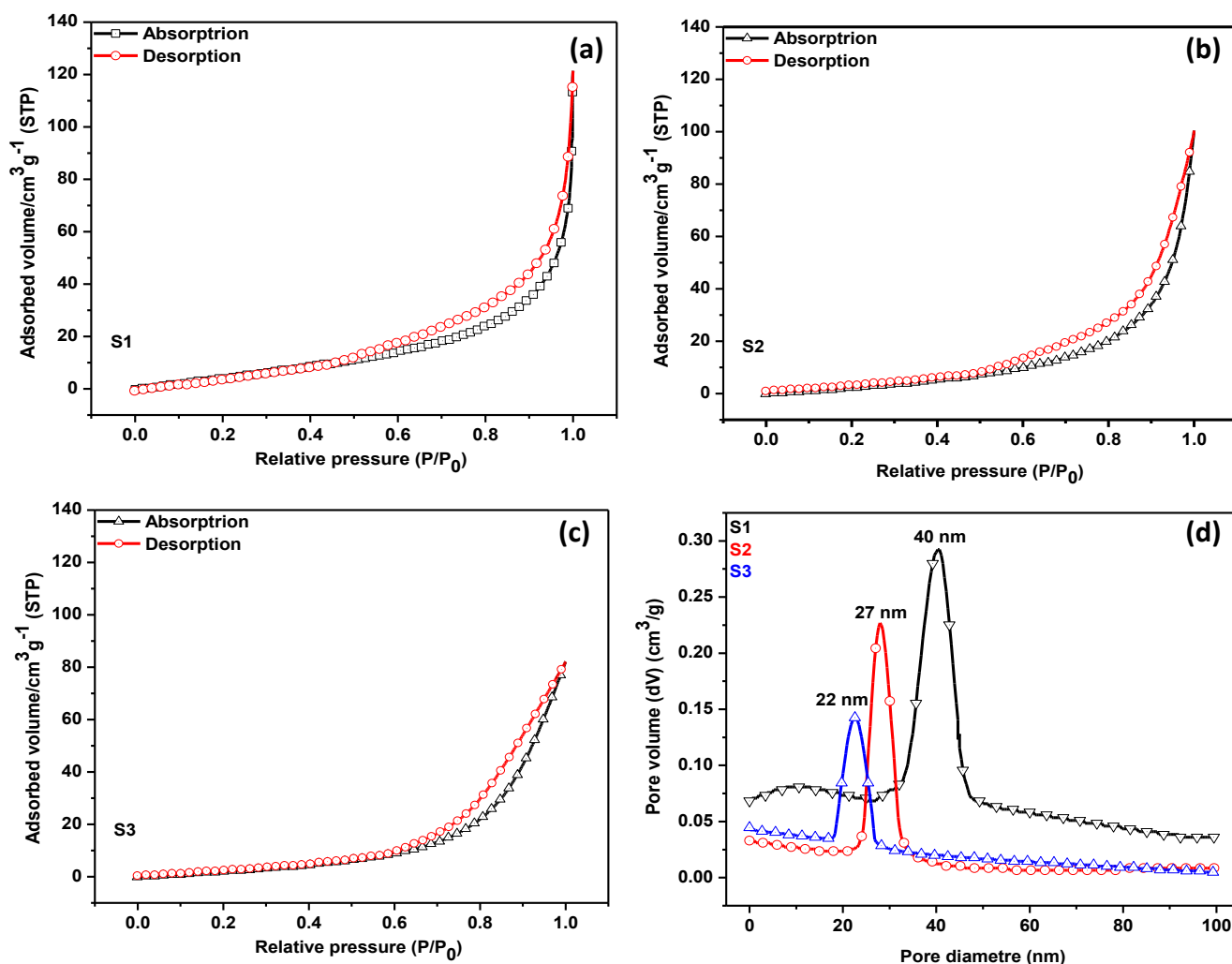
Fig. 4. (a) N_2 adsorption/desorption curve of the prepared samples. (b) Pore-size distribution of the prepared samples.

S1, S2, and S3. First, the reaction mixture is kept in dark and under stirring for 60 min to achieve absorption/desorption equilibrium. After 60 min. all the beakers are exposed to direct sunlight. The aliquots of the dye solutions are collected at regular intervals (20 min.) of time up to 2 h of continuous irradiation. The collected aliquots are regularly subjected to UV–visible spectroscopy at the time of collection, to observe the change in the concentrations of the dye solutions. Fig. 5 (a, b, c) illustrates the graph between C/C_0 and irradiation time for MB, RhB & phenol and also for S1, S2, and S3 samples. From the results, the S1 material shows better performance in the case of both dyes MB and RhB and also for phenol. The reason for this is the larger bandgap of that material among the other two will pave the way for a long time electron-hole separation; hence the conduction band electrons will get enough time to react with molecular oxygen also the holes react with H_2O. The electron-hole recombination rate was lesser for S1 material when compared to S2 and S3, this will be proved in the PL studies. So that it increases the production of active species •OH radicals and O^{2-} anions and thus it will increase the degradation of the material S1. On the other hand from the BET study, it was confirmed that the surface area of the S1 material is higher than that of the S2 and S3. This will promote the number of active sites and also due to the larger pore size a large number of dye molecules were adsorbed on the surface of the material. Hence it will enhance the photocatalytic performance of material S1. Besides these, the crystallite size of the S1 composite is smaller than that of S2 and S3, which also increases the photocatalytic activity.

The order of reaction kinetics and the rate constant of the photo-catalytic reaction was calculated using Langmuir–Hinshelwood relation (Eq. (5)). Fig. 5 (d, e, f) shows the graph between $ln(C/C_0)$ and reaction time for MB, RhB dyes and phenol, from that the rate constant of the reaction was calculated and the reaction follows pseudo-first-order kinetics.

$$ln\left(\frac{c}{c_0}\right) = kt \tag{5}$$

where k is the rate constant and, t is the reaction time. The obtained degradation percentage, and rate constant values of the prepared materials S1, S2, S3 for MB, RhB and phenol were tabulated in the Table 2.

(b) Active species scavenger and reusable experiment:

The active species which play a major role in the dye degradation process was studied using •OH radicals scavenger IPA and O^{2-} anions scavenger PBQ. For this experimental study 0.025 M of PBQ and 2 ml of IPA were added to the dye solution along with catalyst S1, S2, S3 separately. Fig. 6 (a, b) gives detail about the different active species scavengers with S1, S2, and S3 materials for MB and RhB dyes. It is observed that for all the materials and dyes the degradation percentage was drastically decreased for IPA scavenger when compare to PBQ. Hence it is concluded that the majority active species in the degradation process are the •OH radicals in the case of all the three materials. The reusable experiment was done for four repeated cycles, with a newly
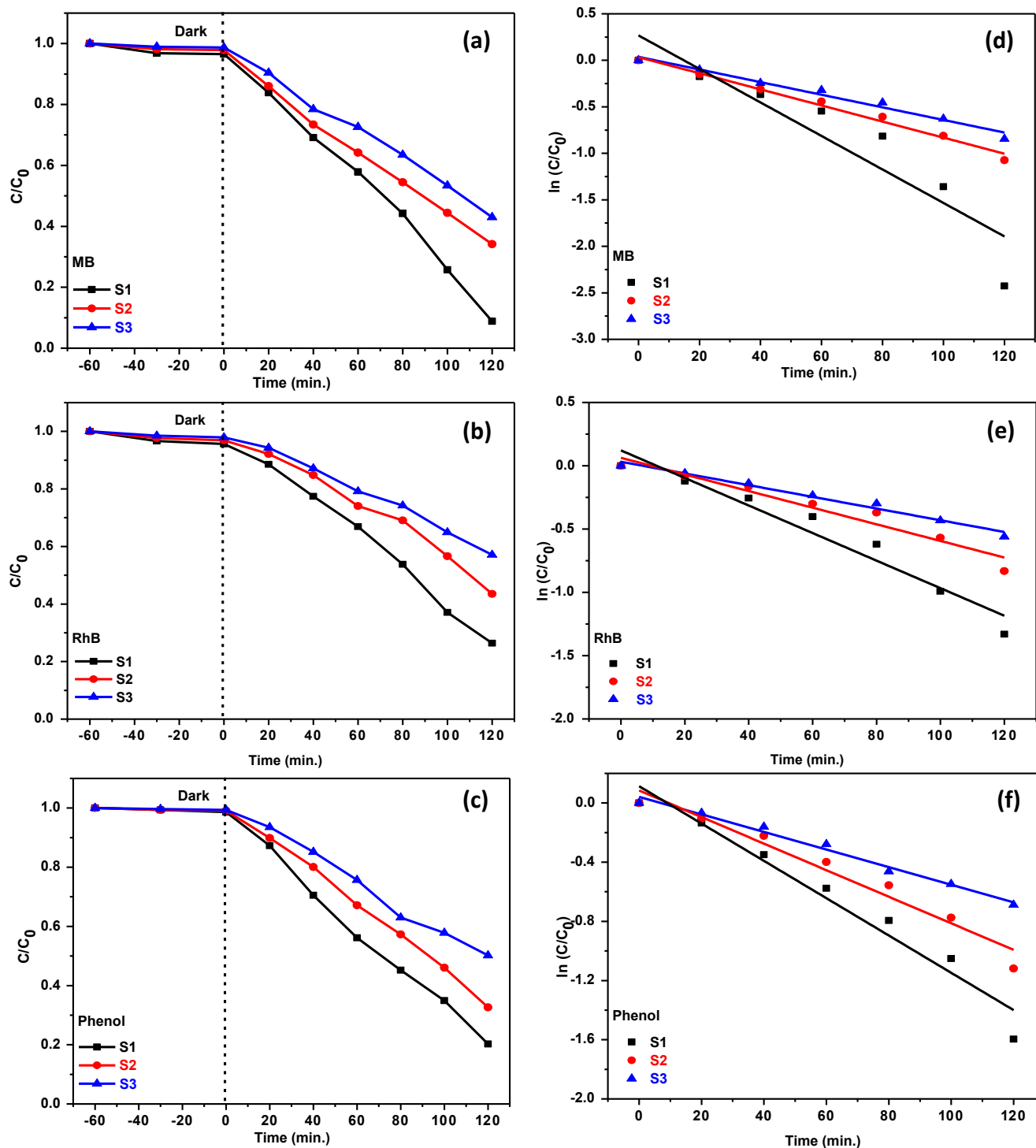
Fig. 5. (a, b, c) Change in concentration Vs irradiation time for MB, RhB and Phenol & (d, e, f) Rate constant for MB, RhB and Phenol.

prepared dye solution for every cycle. The catalyst material was taken and centrifuged, then kept in a hot-air oven for drying after every cycle. Fig. 6 (c, d) shows the withstanding stability of all the prepared samples in the dye degradation process for MB and RhB. From the result, it is noted that the S1 material shows better performance up to three cycles. Fig. 7 (a, b, c) represents the comparative XRD patterns of S1, S2, and S3 samples before and after used in four repeated cycles. From that, it is noted that the predominant peak intensities for all the samples were decreased, which confirms that the synthesis materials get dissociate

due to the continuous and repeated adsorptions of dye molecules on their surfaces. Hence the degradation efficiency of the prepared samples gets diminished after reused.

(c) Mineralization of Dye molecules and phenol:

To determine the mineralization of the pollutants chemical oxygen deficiency (COD) calculations were carried out using titration method [51]. For the calculation of COD, the titrations with Ferrous ammonium

Table 2
Degradation efficiency and rate constant of the prepared samples for MB, RhB and phenol.

Materials	Dye Used	Photocatalytic activity		
		R^2 value	Rate constant (k) ($\times 10^{-3}\,s^{-1}$)	Degradation percentage (%)
Fe$_2$O$_3$@MgO (S1)	MB	0.83057	18.02	91
	RhB	0.93636	10.89	73
	Phenol	0.95044	12.61	79
Fe$_2$O$_3$@Mn$_2$O$_3$ (S2)	MB	0.98462	8.65	65
	RhB	0.93666	6.57	56
	Phenol	0.95344	8.98	67
Fe$_2$O$_3$@Co$_3$O$_4$ (S3)	MB	0.97425	6.78	57
	RhB	0.97825	4.62	42
	Phenol	0.98336	5.95	49

sulfate (FAS) was carried out against the pure DD water, dye solution with initial concentration, and dye solution with final concentration and are formulated by the following formula (Eq. (6)).

Also the percentage of COD for the dye solution and phenol was calculated using the formula (Eq. (7)) and are tabulated in Table 3.

$$\eta = \frac{Initial_{COD} - Final_{COD}}{Initial_{COD}} \times 100(\%) \tag{7}$$

3. Conclusion

The three different composites of Fe$_2$O$_3$ were successfully synthesized through a simple co-precipitation method. The materials phase and composition were confirmed by PXRD, EDAX, and FTIR studies. Optical properties of the samples were studied by UV-DRS and PL spectroscopic techniques. The surface area of the samples is studied by BET technique. The photocatalytic behavior of all the three materials was comparatively analyzed, and the stability of the samples was studied for four repeated cycles. From all the observed results the Fe$_2$O$_3$@MgO composite material shows the extraordinary performance when compare to Fe$_2$O$_3$@Mn$_2$O$_3$ and Fe$_2$O$_3$@Co$_3$O$_4$ composites in the degradation of MB and RhB dyes. Additionally, the radical scavenger

$$COD = \frac{(Blank\ titrate\ value - Dye\ solution\ titrate\ value) \times normality\ of\ FAS \times 8 \times 1000}{Volume\ of\ the\ solution}(ppm) \tag{6}$$
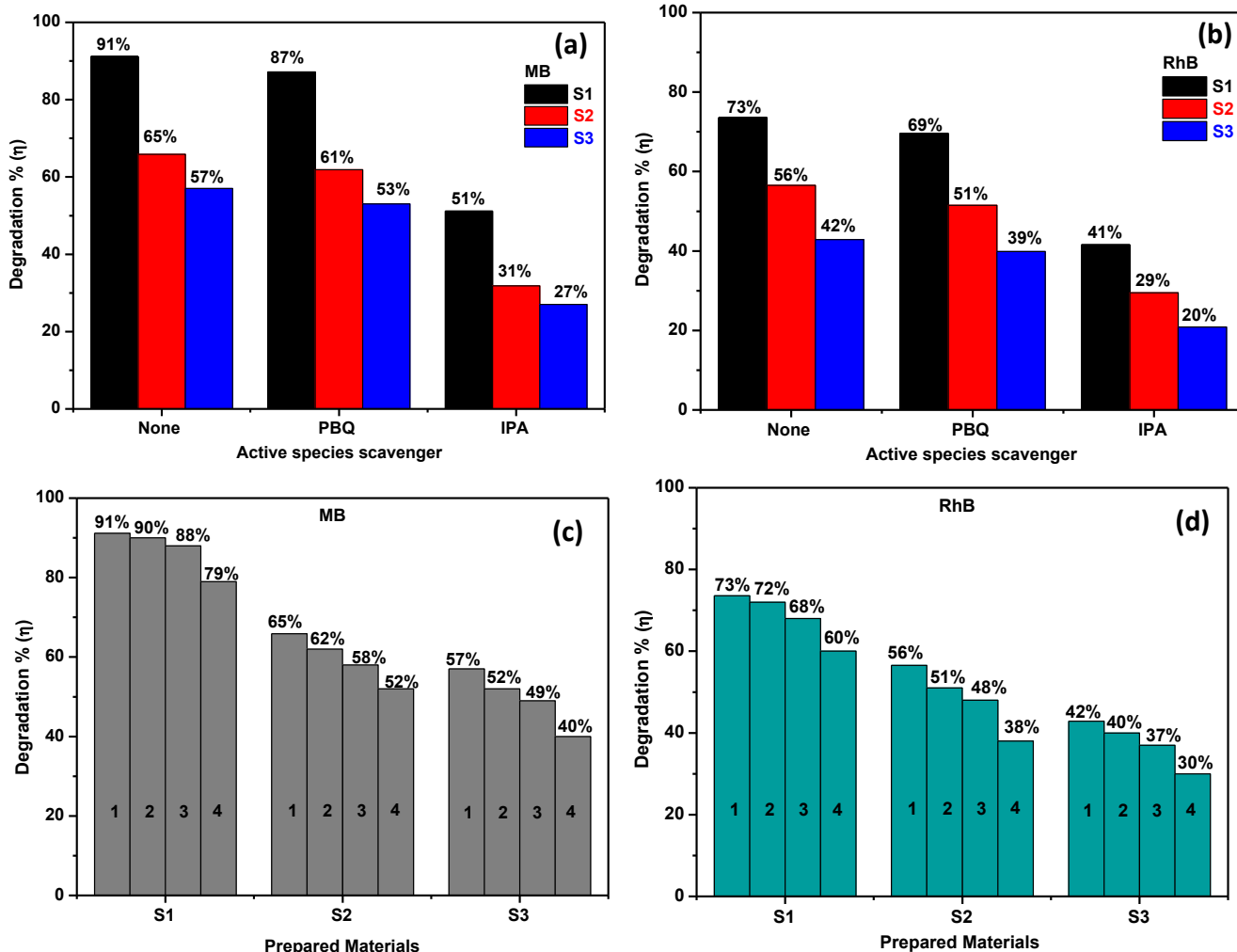

Fig. 6. (a, b) Active species scavenger experiment for MB and RhB dye (c, d) Reusability experiment for MB and RhB dye.
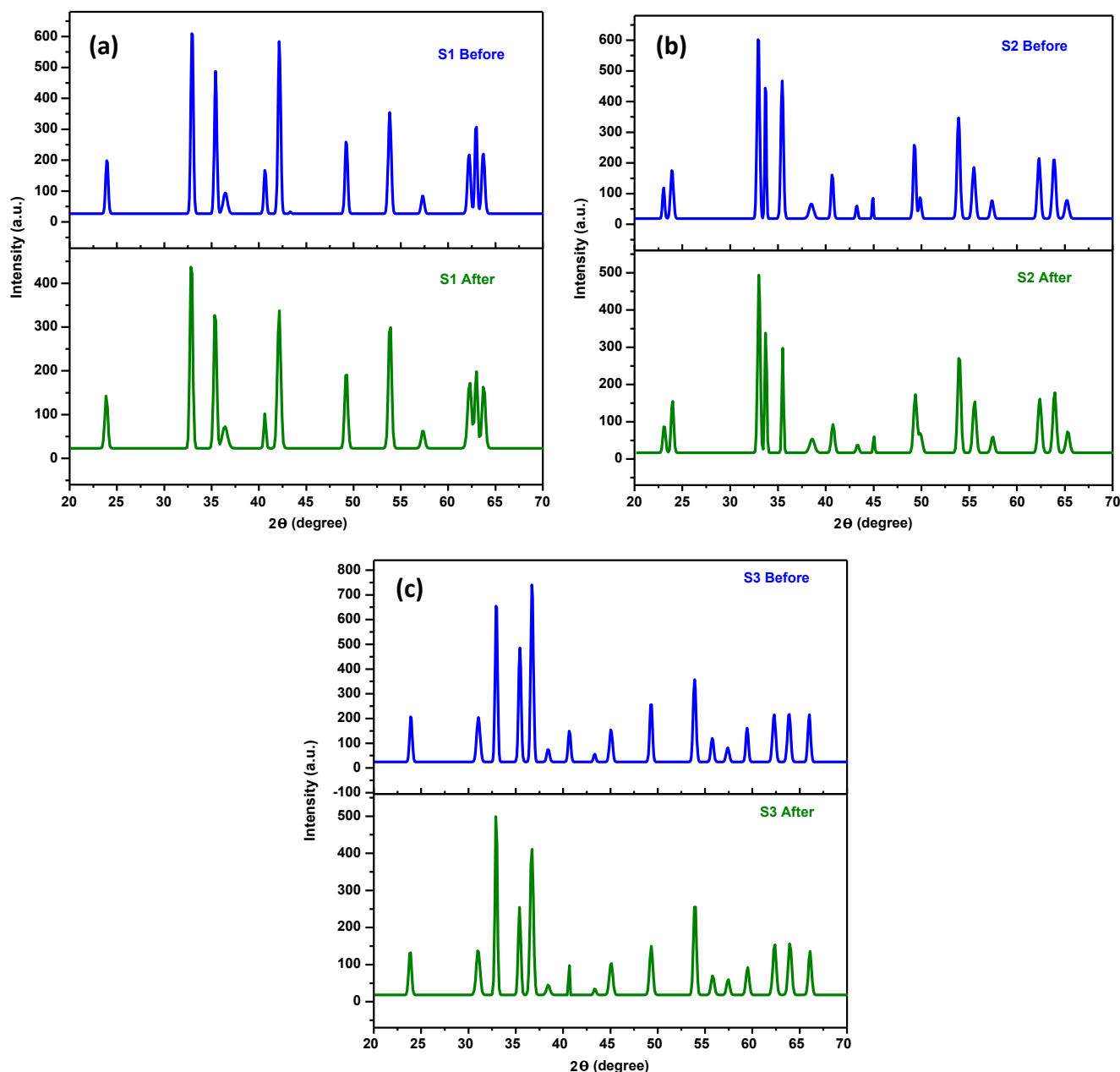
Fig. 7. (a, b, c) PXRD patterns of before and after four cycles for S1, S2, and S3 materials.

Table 3
Percentage of COD removal of the prepared samples for MB, RhB and phenol.

Sample	COD Removal efficiency (%)		
	MB	**RhB**	**Phenol**
S1	83	64	69
S2	54	49	52
S3	51	33	39

experiments are carried out to find the active species. The mineralizations of the organic pollutants are studied and confirmed using COD experiment. The sunlight active photocatalytic activity is also one of the major achievements in this study. Hence the Fe_2O_3@MgO composite material is a suitable nano photocatalyst for the removal of organic pollutants in the wastewater treatments.

Declaration of Competing Interest

The authors declare that they have no known competing financial interests or personal relationships that could have appeared to influence the work reported in this paper.

References

[1] A. Kumar, A. Singlhal. Synthesis of colloidal β-Fe2O3 nanostructures influence of addition of Co2+ on their morphology and magnetic behavior. Nanotechnology 2007;18(47):475703e10.

[2] L. Peng, T. Xie, Y. Lu, H. Fan, D. Wang, Synthesis, photoelectric properties and photocatalytic activity of the Fe2O3/TiO2 heterogeneous photocatalysts, Phys. Chem. Chem. Phys. 12(28) (2010) 8033e41.

[3] L. Wang, H. Wei, Y. Fan, X. Gu, J. Zhan, One-dimensional CdS/α-Fe₂O₃ and CdS/Fe₃O₄ hetero-structures: epitaxial and non-epitaxial growth and photocatalytic activity, J. Phys. Chem. C 113 (32) (2009) 14119–14125.

[4] P. Gregory, Azo dyes: Structure-carcinogenicity relationships, Dyes and Pigments 7 (1986) 45–46.

[5] M.A. Al-Ghouti, M.A. Khraisheh, S.J. Allen, et al., The removal of dyes from textile wastewater: a study of the physical characteristics and adsorption mechanisms of diatomaceous earth, J. Environ. Manage. 69 (3) (2003) 229–238.

[6] X.G. Li, R. Liu, M.R. Huang, Facile synthesis and highly reactive silver ion adsorption of novel micro-particles of sulfo-diphenylamine and diaminonaph copolymers, Chem. Mater. 17 (2005) 5411–5419.

[7] F. He, J.T. Fan, D. Ma, et al., The attachment of Fe_3O_4 nanoparticles to graphene oxide by covalent bonding, Carbon. 48 (2010) 3139–3144.

[8] T.S. Anirudhan, P.L. Divya, J. Nima, S. Sandeep, Synthesis and evaluation of Iron-doped titania/silane based hydrogel for the adsorptional photocatalytic degradation of Victoria blue under visible light, J. Colloid Interface Sci. 434 (2014) 48–58.

[9] M. Pirila, M. Saouabe, S. Ojala, B. Rathnayake, F. Drault, A. Valtanen, M. Huuhtanen, R. Brahmi, R.L. Keiski, Photocatalytic degradation of organic pollutants in wastewater, Top. Catal. 58 (2015) 1085–1099.

[10] S. Naraginti, Y. Li, Y. Wu, Visible light mediated synergistic catalyst for effective inactivation of E. coli and degradation of azo dye Direct Red-22 with mechanism investigation, RSC Adv. 6 (2016) 75724–75735.

[11] S. Dong, L. Xia, T. Guo, F. Zhang, L. Cui, X. Su, J. Sun, Controlled synthesis of flexible graphene aerogels macroscopic monolith as versatile agents for wastewater treatment, Appl. Surface Sci., 445 (2018) 30–38.

[12] S. Dong, X. Ding, T. Guo, X. Yue, X. Han, J. Sun, Self-assembled hollow sphere shaped Bi_2WO_6/RGO composites for efficient sunlight-driven photocatalytic degradation of organic pollutants, Chem. Eng. J. 316 (2017) 778–789.

[13] S. Dong, L. Cui, C. Liu, F. Zhang, K. Li, L. Xia, J. Sun, Fabrication of 3D ultra-light graphene aerogel/Bi_2WO_6 composite with excellent photocatalytic performance: a promising photocatalysts for water purification, J. Taiwan Inst. Chem. Eng. 97 (2019) 288–296.

[14] L. Tan, C. Yu, M. Wang, S. Zhang, J. Sun, S. Dong, J. Sun, Synergistic effect of adsorption and photocatalysis of 3D g-C_3N_4-agar hybrid aerogels, Appl. Surface Sci. 467 (2019) 286–292.

[15] S. Dong, L. Cui, W. Zhang, L. Xia, S. Zhou, C.K. Russell, J. Sun, Double-shelled $ZnSnO_3$ hollow cubes for efficient photocatalytic degradation of antibiotic wastewater, Chem. Eng. J. 384 (2020), 123279.

[16] S. Dong, L. Cui, Y. Tian, L. Xia, Y. Wu, J. Yu, M. Fan, A novel and high-performance double Z-scheme photocatalyst ZnO-SnO2-Zn2SnO4 for effective removal of the biological toxicity of antibiotics, J. Hazardous Mater. 123017 (2020).

[17] K. Huang, Y.H. Li, S. Lin, C. Liang, H. Wang, C.X. Ye, Y.J. Wang, R. Zhang, D. Y. Fan, Y.G. Wang, M. Lei, H.J. Yang, A facile route to reduced graphene oxide–zinc oxide nano rod composites with enhanced photocatalytic activity, Powder Tech. 257 (2014) 113–119.

[18] L. Huang, H. Xu, Y. Li, H. Li, X. Cheng, J. Xia, Y. Xu, G. Cai, Visible-light-induced WO3 /g-C_3N_4 composites with enhanced photocatalytic activity, Dalton Trans. 42 (2013) 8606–8616.

[19] H. Li, J. Liu, W. Hou, N. Du, R. Zhang, X. Tao, Synthesis and characterization of g-C_3N_4 /Bi_2MoO_6 hetero-junctions with enhanced visible light photocatalytic activity, Appl. Catal. B 160–161 (2014) 89–97.

[20] S. Kamal, S. Balu, S. Palanisamy, K. Uma, V. Velusamy, T.C.K. Yang, Synthesis of boron doped C_3N_4 /$NiFe_2O_4$ nanocomposite: an enhanced visible light photo-catalyst for the degradation of methylene blue, Results Phys. 12 (2019) 1238–1244.

[21] W. Guo, K. Fan, J. Zhang, C. Xu, 2D/2D Z-scheme Bi_2WO_6 /Porous-g-C_3N_4 with synergy of adsorption and visible-light-driven photodegradation, Appl. Surf. Sci. 447 (2018) 125–134.

[22] S.G. Kumar, L.G. Devi, Review on modified TiO_2 photocatalysis under UV/visible light: selected results and related mechanisms on interfacial charge carrier transfer dynamics, J. Phys. Chem. A 115 (2011) 13211–13241.

[23] Y. Shi, H. Li, L. Wang, W. Shen, H. Chen, Novel α-Fe_2O_3/CdS corn-like nanorods with enhanced photocatalytic performance, ACS Appl. Mater interfaces 4 (9) (2012) 4800–4806.

[24] M. Yadav, K.Y. Rhee, S.J. Park, D. Hui, Mechanical properties of Fe_3O_4/GO/chitosan composites, Compos. Part B Eng. 66 (2014) 89–96.

[25] J. Liu, S. Yang, W. Wu, Q. Tian, S. Cui, Z. Dai, C. Jiang, 3D flowerlike α-Fe_2O_3@TiO_2 core–shell nanostructures: general synthesis and enhanced photocatalytic performance, ACS Sustain. Chem. Eng. 3 (11) (2015) 2975–2984.

[26] J. Xie, Z. Zhou, Y. Lian, Y. Hao, P. Li, Y. Wei, Synthesis of α-Fe_2O_3/ZnO composites for photocatalytic degradation of pentachlorophenol under UV–vis light irradiation, Ceram. Int. 41 (2) (2015) 2622–2625.

[27] S. Frindy, M. Sillanpää, Synthesis and application of novel α-Fe_2O_3/graphene for visible-light enhanced photocatalytic degradation of RhB, Mater. Des. 188 (2020), 108461.

[28] S. Jorfi, G. Barzegar, M. Ahmadi, R.D.C. Soltani, A. Takdastan, R. Saeedi, M. Abtahi, Enhanced coagulation-photocatalytic treatment of Acid red 73 dye and real textile wastewater using UVA/synthesized MgO nanoparticles, J. Environ. Manage. 177 (2016) 111–118.

[29] K. Mageshwari, S.S. Mali, R. Sathyamoorthy, P.S. Patil, Template-free synthesis of MgO nanoparticles for effective photocatalytic applications, Powder Technol. 249 (2013) 456–462.

[30] S. Chandra, P. Das, S. Bag, R. Bhar, P. Pramanik, Mn_2O_3 decorated graphene nanosheet: an advanced material for the photocatalytic degradation of organic dyes, Mater. Sci. Eng.: B 177 (11) (2012) 855–861.

[31] S. Gnanam, V. Rajendran, Facile hydrothermal synthesis of alpha manganese sesquioxide (α-Mn_2O_3) nanodumb-bells: structural, magnetic, optical and photocatalytic properties, J. Alloys Compounds 550 (2013) 463–470.

[32] X. Lou, J. Han, W. Chu, X. Wang, Q. Cheng, Synthesis and photocatalytic property of Co_3O_4 nanorods, Mater. Sci. Eng.: B 137 (1–3) (2007) 268–271.

[33] H. Li, G.T. Fei, M. Fang, P. Cui, X. Guo, P. Yan, L. De Zhang, Synthesis of urchin-like Co_3O_4 hierarchical micro/nanostructures and their photocatalytic activity, Appl. Surface Sci. 257 (15) (2011) 6527–6530.

[34] R. Wahab, F. Khan, A.A. Al-Khedhairy, Hematite iron oxide nanoparticles: apoptosis of myoblast cancer cells and their arithmetical assessment, RSC Adv. 8 (44) (2018) 24750–24759.

[35] K.R. Nemade, waghuley, d. S. Synthesis of MgO nanoparticles by solvent mixed spray pyrolysis technique for optical investigation, Int. J. Met, 1 (2014).

[36] W. Feng-Ping, M.Y. Rafique, A.M. Toufiq, M.Z. Iqbal, Canted antiferromagnetic and optical properties of nanostructures of Mn_2O_3 prepared by hydrothermal synthesis, Chinese Phys. B 21 (11) (2012), 117311.

[37] R. Bhargava, S. Khan, N. Ahmad, & M. M. N. Ansari, Investigation of structural, optical and electrical properties of Co3O4 nanoparticles, in: AIP Conference Proceedings (Vol. 1953, No. 1, p. 030034). AIP Publishing LLC, 2018.

[38] S.W. Hwang, A. Umar, G.N. Dar, S.H. Kim, R.I. Badran, Synthesis and characterization of iron oxide nanoparticles for phenyl hydrazine sensor applications, Sens. Lett. 12 (1) (2014) 97–101.

[39] W.B. Carpenter, J.A. Fournier, R. Biswas, G.A. Voth, A. Tokmakoff, Delocalization and stretch-bend mixing of the HOH bend in liquid water, J. Chem. Phys. 147 (8) (2017), 084503.

[40] I.W. Sutapa, A.W. Wahab, P. Taba, N. La Nafie, Synthesis and structural profile analysis of the MgO nanoparticles produced through the sol-gel method followed by annealing process, Orient. J. Chem. 34 (2) (2018) 1016–1025.

[41] M. Pudukudy, Z. Yaakob, Synthesis, characterization, and photocatalytic performance of mesoporous α-Mn2O3 microspheres prepared via a precipitation route, J. Nanoparticles (2016).

[42] I.C. Alves, J. Santos, D.S. Viégas, E.P. Marques, C.A. Lacerda, L. Zhang, A. L. Marques, Nanoparticles of Fe_2O_3 and Co_3O_4 as efficient electrocatalysts for oxygen reduction reaction in acid medium, J. Braz. Chem. Soc. 30 (12) (2019) 2681–2691.

[43] P. Mallick, B.N. Dash, X-ray diffraction and UV-visible characterizations of α-Fe_2O_3 nanoparticles annealed at different temperature, J. Nanosci. Nanotechnol 3 (5) (2013) 130–134.

[44] S.A. Makhlouf, Z.H. Bakr, K.I. Aly, M.S. Moustafa, Structural, electrical and optical properties of Co_3O_4 nanoparticles, Superlattices Microstruct. 64 (2013) 107–117.

[45] M. Sharrouf, R. Awad, M. Roumié, S. Marhaba, Structural, optical and room temperature magnetic study of Mn_2O_3 nanoparticles, Mater. Sci. Appl. 6 (10) (2015) 850.

[46] A. Almontasser, A. Parveen, A. Azam, Synthesis, characterization and antibacterial activity of Magnesium Oxide (MgO) nanoparticles, In: IOP Conference Series: Materials Science and Engineering (Vol. 577, No. 1, p. 012051). IOP Publishing, 2019.

[47] Z.L. Wang, Zinc oxide nanostructures: growth, properties and applications, J. Phys.: Condens. Matt. 16 (25) (2004) R829.

[48] R.K. Sendi, S. Mahmudm, Quantum size effect on ZnO nanoparticle-based discs synthesized by mechanical milling, Appl. Surf. Sci. 258 (2012) 8026–8031.

[49] X.L. Wu, G.G. Siu, C.L. Fu, H.C. Ong, Photoluminescence and cathode-luminescence studies of stoichiometric and oxygen-deficient ZnO films, Appl. Phys. Lett. 78 (16) (2001) 2285–2287.

[50] A.E. Reddy, T. Anitha, C.V. Gopi, S.S. Rao, C.V. Thulasi-Varma, D. Punnoose, H. J. Kim, Fabrication of a snail shell-like structured MnO 2@ CoNiO2 composite electrode for high performance supercapacitors, RSC Adv. 7 (20) (2017) 12301–12308.

[51] K. Ravichandran, K.S. Seelan, P. Kavitha, S. Sriram, Influence of Cu+ g-C_3N_4 incorporation on the photocatalytic dye decomposition of ZnO film coated on stainless steel wire meshes, J. Mater. Sci.: Mater. Electron. 30 (22) (2019) 19703–19717.